ORIGINAL ARTICLE

Modeling on *in vivo* disposition and cellular transportation of RNA lipid nanoparticles *via* quantum mechanics/physiologically-based pharmacokinetic approaches

Wei Wang[a,b], Shiwei Deng[a,b], Jinzhong Lin[c,d,e], Defang Ouyang[a,b,*]

[a]State Key Laboratory of Quality Research in Chinese Medicine, Institute of Chinese Medical Sciences, University of Macau, Macau 999078, China
[b]Faculty of Health Sciences, University of Macau, Macau 999078, China
[c]State Key Laboratory of Genetic Engineering, School of Life Sciences, Fudan University, Shanghai 200438, China
[d]Center for mRNA Translational Research, Fudan University, Shanghai 200438, China
[e]Zhangjiang mRNA Innovation and Translation Center, Fudan University, Shanghai 200438, China

Abstract   The lipid nanoparticle (LNP) has been so far proven as a strongly effective delivery system for mRNA and siRNA. However, the mechanisms of LNP's distribution, metabolism, and elimination are complicated, while the transportation and pharmacokinetics (PK) of LNP are just sparsely investigated and simply described. This study aimed to build a model for the transportation of RNA-LNP in Hela cells, rats, mice, and humans by physiologically based pharmacokinetic (PBPK) and quantum mechanics (QM) models with integrated multi-source data. LNPs with different ionizable lipids, particle sizes, and doses were modeled and compared by recognizing their critical parameters dominating PK. Some interesting results were found by the models. For example, the metabolism of ionizable lipids was first limited by the LNP disassembly rate instead of the hydrolyzation of ionizable lipids; the ability of RNA release from endosomes for three ionizable lipids was quantitively derived and can predict the probability of RNA release. Moreover, the biodegradability of three ionizable lipids was estimated by the QM method and the is generally consistent with the result of PBPK result. In summary, the transportation model of RNA LNP among various species for the first time was successfully constructed. Various *in vitro* and *in vivo* pieces of evidence were integrated through QM/PBPK multi-level modeling. The resulting new understandings are related to biodegradability, safety, and RNA release ability which are highly concerned issues of the formulation. This would benefit the design and research of RNA-LNP in the future.

1. Introduction

The lipid nanoparticle (LNP) is a powerful delivery system for nucleic acid therapy. Its application led to the approval of the first siRNA drug (Onpattro®) for treating the polyneuropathy of hereditary transthyretin-mediated amyloidosis in adults[1] and the first two mRNA vaccines (Comirnaty® and Spikevax®) against COVID-19[2,3]. Upon injection, LNP protects nucleic acids from biodegradation and conveys them into the endosomes of target cells. Then, nucleic acids escape from endosomes and have their intended effects, down-regulating (siRNA-LNP) or up-regulating (mRNA-LNP) protein expression[4].

A typical LNP contains four lipid ingredients, including ionizable lipids, cholesterol, phospholipids lipids, and polyethylene glycol (PEG) lipids[5]. They account for the percentage in typical LNP formulations at around 50, 38.5, 10, and 1.5, respectively. Ionizable lipids can be positively charged in acidic conditions, which promotes RNA encapsulation and the interaction between LNP and endosomal membranes through electrostatic interaction. The other three types of lipids take the role of modulating membrane fluidity, stabilizing particles, controlling particle size, and helping endocytosis of LNPs[6].

The use of ionizable lipids is the most striking feature of LNP, endowing it with unique *in vivo* processes. Upon injection, LNPs are discharged in neutral plasma, allowing adsorption of plasma proteins onto particle surface and the following cellular uptake mediated by receptors on cells[6,7]. Then, LNPs are transferred *via* endosomes, wherein they become positively charged due to the acidic environment, interacting with and disrupting endosomal membranes, resulting in RNA release into the cytoplasm. Meanwhile, LNPs disassemble and the remaining lipids are transferred to lysosomes or autolysosomes[8,9] and undergo the metabolism route[10].

The multi-steps of LNP transportation in the body complicates the investigation of its pharmacokinetic (PK) properties. For drug development, PK is important since around 80 percent of drugs fail in clinical may due to PK-related issues[11]. Therefore, nowadays a deep understanding of PK and its impacting factors is stressed in advanced drug development strategies[12]. However, due to the complexity, the PK of LNPs is commonly simply described as a bulk reflected by concentration *versus* time profiles[10,13−15]. Although research deeply focusing on some steps of transportation has been reported, this approach inevitably results in isolated knowledge about PK behaviors[8,9,16,17]. Thus, better tools are needed to promote the PK analysis for RNA-LNP formulations by integrating multi-source data and characterizing or predicting kinetic properties for each step of LNP transportation. Based on this, formulations can be compared and optimized.

Modeling is a useful approach to achieve this goal. The physiologically-based pharmacokinetic (PBPK) model is an advanced mechanistic modeling method that simulates the PK based on physiological and pharmaceutical parameters[18]. Currently, wide applications of PBPK to formulation development and medication regimen recommendation have been reported[19] and its usage is recommended by regulatory agencies[12,20]. In RNA therapy, the PBPK method has been used in the simulation of the disposition of an *N*-acetylgalactosamine-conjugated siRNA[21]. For LNP formulation, a model was built to simulate the PK of intramuscularly injected LNP[22]. The model focuses on the transfer of LNP *via* the lymphatic route to plasma, but the model structure of systemic circulation is simple, and only one formulation was investigated.

Quantum mechanics (QM) is another commonly applied modeling method in drug discovery, especially simulating drug metabolism[23]. QM is an ab initio method that simulates the interaction between molecules and atoms based on their electronic structures calculated *via* the Schrodinger equation and wave function. Thus, it can be used to investigate chemical reactions from a microscopic and mechanistic view. In the LNP system, the metabolism of ionizable lipids is a concern since it is the major ingredient in the formulation and low biodegradability is likely to induce toxicity due to lipid accumulation[24]. If the metabolism process can be simulated and biodegradability can be assessed by the modeling method, it would promote the development of ionizable lipids and LNP formulation.

In this study, PBPK models were constructed to simulate RNA-LNP delivery in Hela cells, rats, mice, and humans. In the animal models, we focused on the PK of ionizable lipids, while in the cell model, the PK of both RNA and ionizable lipids was simulated simultaneously. The modeling aimed to disintegrate the PK of LNPs into several steps and recognize their rate values. Besides, QM modeling was conducted to simulate the metabolism of ionizable lipids in the rats. Energy change of three lipids, DLin-MC3-DMA (MC3), SM-102, and Lipid 5, during catalyzation by esterase[13,15] were calculated as the surrogate of biodegradability and compared to the result from PBPK. By doing this multi-level modeling (Fig. 1), we quantitatively compared the behaviors of LNPs at multiple phases in PK and explained some experimental observations mechanistically.

2. Materials and methods

2.1. PBPK modeling on in vivo disposition of RNA-LNP

2.1.1. Data collection

Various PK data were collected to help the building of PBPK models for rats[13,25], mice[14,16], and humans[26]. In the rat study[13,25], Sprague−Dawley rats at 225−250 g in body weight were intravenously administered with human erythropoietin (hEPO) encoding mRNA-LNPs at the dose of 0.2 mg/kg dose mRNA. The LNP was composed of ionizable lipids, DSPC, cholesterol, and PEG-lipid at the molar ratio of 50:10:38.5:1.5. The ratio of nitrogen in the ionizable lipid and phosphate in the mRNA backbone (*N/P* ratio) was estimated as 5.67 according to the research from the same company[24]. The ionizable lipids used included MC3, SM-102, and Lipid 5[13] (Supporting Information Fig. S1). In one mouse study[16], 6−8 week CD-1 mice were intravenously administered with siRNA-LNP silencing the gene FVII at the lipid dose of 0.33, 3.3, and 11.1 mg/kg. The dose and exposure presented a linear relationship. The LNP was composed of MC3, DSPC, cholesterol, and PEG-lipid at the molar ratio of 50:10:38.5:1.5, and the weight ratio of total lipid to siRNA was around 10:1. In another mouse study[14], 6−8 week old C57BL/6
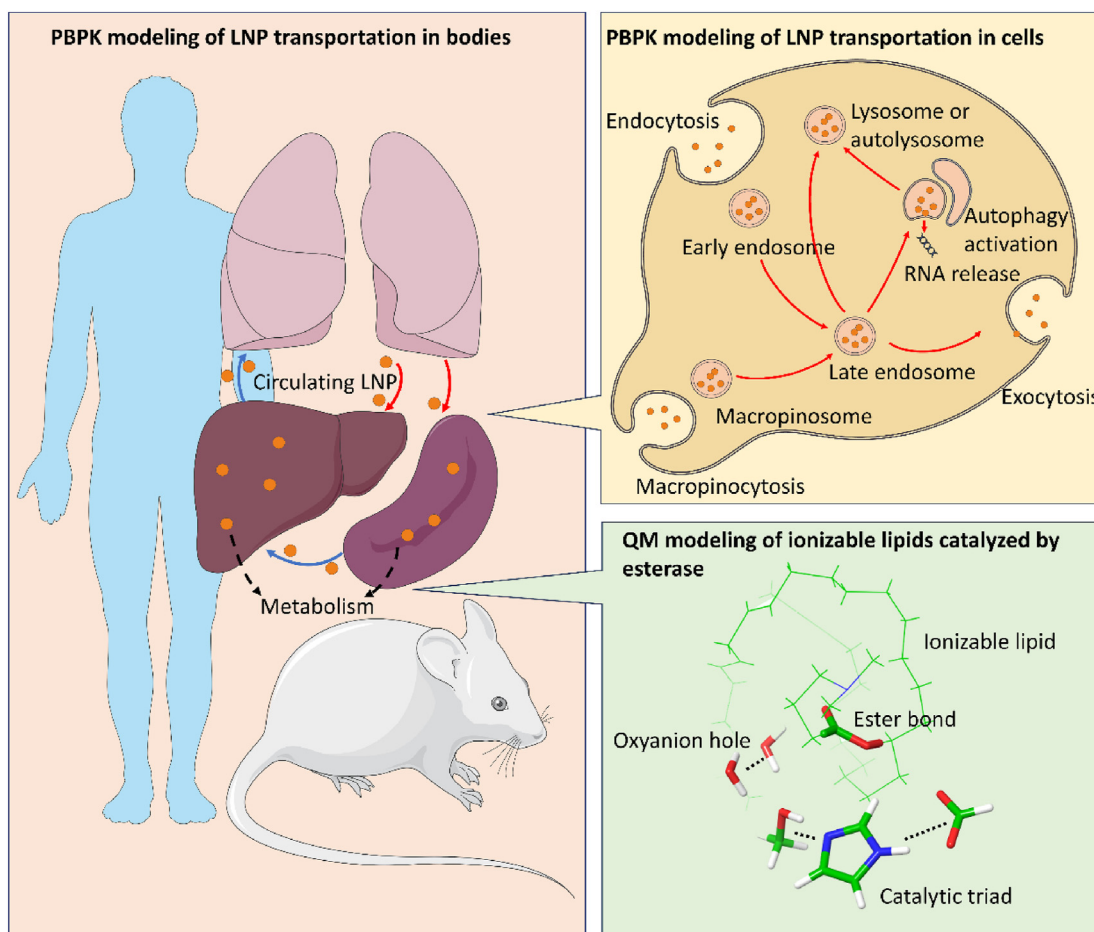
Figure 1 PBPK and QM modeling of RNA-LNP transportation and metabolism. PK profiles of ionizable lipids in LNP were modeled through the PBPK model by simulating their transportation and metabolism in different organs. The transportation of RNA-LNP in cells was also modeled through a cellular PBPK model by simulating their uptake, transportation along endosomes, exocytosis, and RNA release. The metabolism of ionizable lipid by esterase (hydrolysis of the ester bond) was modeled by QM modeling through a cluster approach focusing on the reaction in the active site that is composed of a catalytic triad and an oxyanion hole provided by the esterase.

mice were intravenously administered with siRNA at 0.3 mg/kg loaded in similarly composed LNP. The used ionizable lipid was DMAP-BLP which is an analog to MC3. The proportion that PEG-lipid accounted for ranged from 0.25% to 5% to produce LNP with different particle sizes, while the *N/P* ratios used were three and six. The human data collected is from the phase 1 clinical trials (ALN-TTR02-001 and ALN-TTR02-005) of the first approved siRNA drug (patisiran or Onpattro®)[26]. In the trial, healthy volunteers were intravenously administered 0.5, 0.3, 0.15, 0.05, and 0.01 mg/kg doses of patisiran. Its LNP formulation is very similar to that in the above mouse study[16].

With information about doses of RNA, composition ratios in ingredients, and the age or weight of subjects, it can calculate the corresponding doses of ionizable lipids administered and allow PK modeling.

2.1.2. Model structure, equations, and parameters

The PBPK model of RNA-LNP stressed the behaviors of ionizable lipids. The model was built with MATLAB SimBiology APP (The MathWorks, Inc., Natick, MA, USA) in the 2022a version. To balance the reality and solvability of the model, a series of model structures were built and fitted to the MC3-LNP data[13] to find the optimal one (Supporting Information Fig. S2). Eventually, the

model structure was optimized as Fig. 2. The whole body was divided into six main compartments, including the vein, artery, lung blood vessel, liver, spleen, and "other organs". The distribution of lipids in the liver and spleen was specifically modeled since they are the main target organs of LNPs[14].

Each link in the model structure is modeled as an ordinary differential equation (ODE) which defines the lipid mass transfer rate due to a specific process. For example, in the liver, the lipid transfer is composed of the following elements as in Eqs. (1)−(6):

From artery to organ blood through blood flow:
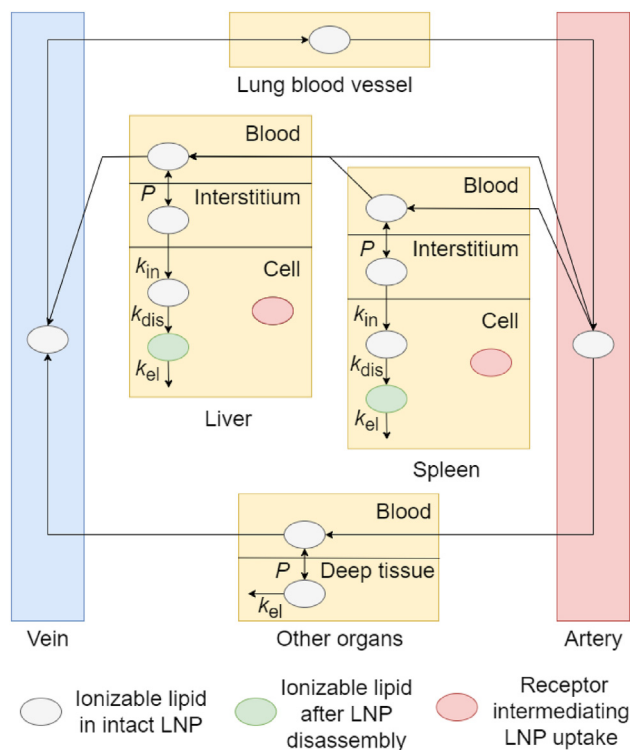
$$\frac{dM_{art\_org}}{dt} = Q \cdot C_{art} \tag{1}$$

From organ blood to vein through blood flow:

$$\frac{dM_{org\_vein}}{dt} = Q \cdot C_{blood} \tag{2}$$

From organ blood to interstitium through permeation:

$$\frac{dM_{blood\_inter}}{dt} = P \cdot S \cdot (C_{blood} - C_{inter}) \tag{3}$$

From interstitium to intracellular space through receptor-mediated internalization:

Figure 2 The optimized PBPK model structure of the ionizable lipid PK in the RNA-LNP delivery system. The ionizable lipid was distributed in the circulating system and to all organs in the form of LNP up to its disassembly and then was metabolized. P, permeability; k_{in}, cellular uptake rate of LNP; k_{dis}, LNP disassembly rate to release free ionizable lipids; k_{el}, metabolism rate of the ionizable lipid.

$$\frac{dM_{inter\_intact}}{dt} = k_{in} \cdot C_{inter} \cdot C_{receptor} \cdot V_{inter} \tag{4}$$

LNP disassembly forming free ionizable lipids:

$$\frac{dM_{intact\_free}}{dt} = k_{dis} \cdot C_{cell} \cdot V_{cell} \tag{5}$$

Metabolism of free ionizable lipids:

$$\frac{dM_{free\_meta}}{dt} = k_{el} \cdot C_{cell} \cdot V_{cell} \tag{6}$$

dM/dt (mg/h) means the mass change at a short time unit, which is the change rate. Q (mL/h) is the blood flow. All C symbols (mg/mL) except for $C_{receptor}$ indicate lipid concentrations in specific compartments. $C_{receptor}$ (mmol/mL) is the concentration of the receptor intermediating LNP uptake. Similarly, all V symbols (mL) present the volume of various organs or sub-organs. P (cm/s) is the permeability of LNP and S (cm^2) is the endothelium surface of an organ, and the product of them is the rate parameter indicating lipid amount exchange between blood and interstitial space of an organ. k_{in} (mL/mmol/h) is the cellular uptake rate relying on the concentration of lipids and receptors according to the chemical kinetic law. k_{dis} (1/h) is the LNP disassembly rate to release free ionizable lipids. k_{el} (1/h) is the metabolism rate at which the ionizable lipid is hydrolyzed.

The ODE representing the change of lipid mass in a specific compartment is the sum of the change rates associated with the compartment considering the change direction. For example, the ODE for mass change in the liver blood is calculated as in Eq. (7):

$$\frac{dM_{blood}}{dt} = \frac{dM_{art\_org}}{dt} - \frac{dM_{org\_vein}}{dt} - \frac{dM_{blood\_inter}}{dt} \tag{7}$$

Because there is an influx of lipids from artery blood and effluxes to the interstitium and vein blood for the liver blood compartment. The ODEs representing lipid mass change in all compartments constitute the PBPK model, which are presented in the Supporting Information.

The model requires physiological parameters such as organ volumes and blood flows as input. To obtain these parameters, growth curves of animals (such as from Charles River Laboratories) and the database of another PBPK modeling software, PK-Sim 11 (Open System Pharmacology, https://www.open-systems-pharmacology.org/) were referred to. The collected parameters are shown in Table 1.

Before performing the PBPK simulation, the lipid mass in the vein was initialized as the dose for intravenous administration, and the mass in all other compartments was zero.

2.1.3. Model fitting and simulation

To characterize pharmaceutically related parameters for different data sources, the model was modified accordingly to fit them. In the rat PK data, LNPs containing ionizable lipids of MC3, SM-102, and Lipid 5 were tested[13], MC3 was deemed the standard and the other two were compared to it based on scaling factors as in Eq. (8):

$$X = X_{MC3} \cdot Scale_X (X \; is \; k_{in}, k_{dis}, or \; k_{el}) \tag{8}$$

LNP cellular uptake is dependent on receptor concentration in the liver and spleen. Since no accurate concentration of the receptor in tissues was found, the receptor concentration in the liver was assumed to be 1 mmol/mL and scaled to that in the spleen as in Eq. (9):

$$C_{receptor\_spleen} = C_{receptor\_liver} \cdot Scale_{receptor} \tag{9}$$

Although accurate values of parameter X and receptor concentration cannot be determined in this study, the design of scaling factors still allows the comparison between LNPs.

For mice data, due to the limitations of the experimental design, only the processes up to distribution to organs can be parameterized[14,16]. Thus, a model shutting off the process of LNP disassembly and hydrolyzation in the liver and spleen was used. Additionally, for the data of DMAP-BLP containing LNP[14], the dissociation process of ionizable lipid from LNP was added to every blood and interstitium compartment, and an additional simulation was performed. For the fitting to human data[26], the model was further reduced by shutting off the LNP entry into the spleen and the elimination route in the "other" compartment due to the issue of data size and model solvability.

In the fitting, the default estimation method "lsqnonlin" was chosen to fit the parameters. Four error models, "constant", "proportional", "exponential", and "combined", were compared to obtain the best performance model. Fitting results were validated mainly by our inspection and by Bayesian information criterion (BIC), Akaike information criterion (AIC), and log-likelihood.

Table 1 Physiological parameters used in the *in vivo* PBPK.

Parameter	Unit	Rat	Mice	Human
Body weight	kg	0.2375	0.0270	69.70
Liver	mL	10.74	1.230	2350
Lung	mL	1.040	0.0947	1200
Other	mL	216.6	18.90	63,760
Spleen	mL	0.6260	0.0950	210.0
Vein	mL	7.830	0.5700	1480
Artery	mL	3.840	0.2900	940.0
Liver blood vessel	mL	1.289	0.1476	399.5
Liver cell	mL	7.733	0.8856	1574
Liver interstitium	mL	1.718	0.1968	376.0
Spleen blood vessel	mL	0.1753	0.02520	69.30
Spleen interstitium	mL	0.09390	0.01350	31.50
Spleen cell	mL	0.3568	0.05130	109.2
Other organs' blood vessel	mL	7.043	0.6855	2055
Other organs' cell	mL	209.5	18.22	61,710
Lung blood vessel	mL	0.6552	0.05670	696.0
Hepatic artery blood flow[a]	mL/h	697.7	114.3	88,200
Hepatic vein blood flow	mL/h	737.3	119.4	98,400
Lung blood flow	mL/h	2400	310.8	360,000
Other organs' blood flow	mL/h	1663	191.4	261,600
Spleen blood flow	mL/h	39.60	5.100	10,200
Liver endothelium surface area	cm^2	1173	134.5	378,900
Spleen endothelium surface area	cm^2	167.6	25.37	64,650
Other organs' endothelium surface area	cm^2	6123	589.9	1,805,000
Hematocrit	Dimensionless	0.4500	0.4500	0.4700
Receptor concentration in liver[b]	mmol/mL	1.000	1.000	−
Receptor scaling from the liver to spleen[b]	Dimensionless	0.3729	0.1217	−

−, not applicable.

[a]The value of "hepatic artery blood flow" is the sum of blood flows through the hepatic artery, large intestine, small intestine, and pancreas.

[b]The "receptor concentration in the liver" is assumed to be 1, and the "receptor scaling from the liver to spleen" is the fold difference of receptor concentration between the liver and spleen that was determined by fitting to PK data.

## 2.2. PBPK modeling on cellular transportation of RNA-LNP

2.2.1. Data collection

The data of LNP transportation and RNA release in Hela cells of three ionizable lipids, C12-200, MC3, and L319, were collected to develop the cellular PBPK model[8,9,17]. After summarizing these investigations, a route of LNP transportation in cells can be described. LNP is first taken up into the early endosome or the macropinosome through the intermediation of various receptors. Then some exchanges of proteins take place between the endosome or macropinosome and the cell and promote their maturing to form the late endosome and further the lysosome. After uptake, LNP starts to disassemble. In the stage of the late endosome, a considerable proportion of LNP would be secreted to the outside of the cell through moving vesicles. Meanwhile, a small proportion of LNP contained in the late endosome triggers the RNA release event. However, only fractional RNA loaded in the LNP can be released into the cytoplasm even if release happens. After the release event, the late endosome would be wrapped by autophagosome and then integrated into autolysosome. In the research of C12-200, cellular LNP uptake, disassembly, and egress out of cells were investigated[9]. In the research of MC3, time courses of LNP uptake, the fractions of two types of endosomes and lysosomes, and the fraction of siRNA release in relation to the amount of uptake are available[17]. In the research of L319, data was presented on LNP uptake, the proportion of vesicles that triggered the release event, and the proportion of siRNA that was released and remained in endosomes[8].

2.2.2. Model structures, equations, and parameters

The cellular PBPK model was also built with MATLAB SimBiology APP (The MathWorks, Inc.) 2022a version. According to the LNP transportation mechanism in Hela cells mentioned above, two versions of PBPK model structures were built, as shown in Fig. 3. The complex model structure is a most mechanistic model that presents the mechanisms of LNP transportation in detail. However, the complex model may be too specialized and not universal since the disassembly of LNP was not commonly investigated in research. Therefore, a reduced model where the LNP disassembly was not explicitly simulated was also built. Some processes were not considered in the modeling work because they were not the main focus of the study or were not investigated due to the limitations of the experimental methodology in the original studies. The processes omitted include LNP disassembly in the culture medium, egress of intact LNP out of cells, re-uptake of disassociated lipids and RNA, and metabolism of lipids and RNA.

Similarly, all functions used in MATLAB SimBiology (The MathWorks, Inc.) are presented in the Supporting Information. A parameter of weight ratio was involved to describe the mass of lipid and RNA in the LNP incubated with Hela cells at the initial state. The process of LNP uptake was modeled as a function of time which was fitted as the uptake profile presented in the original data. The mass change due to other processes was modeled with first-order kinetic parameters shown in the following Eqs. (10)−(17):

Complex model

Reduced model
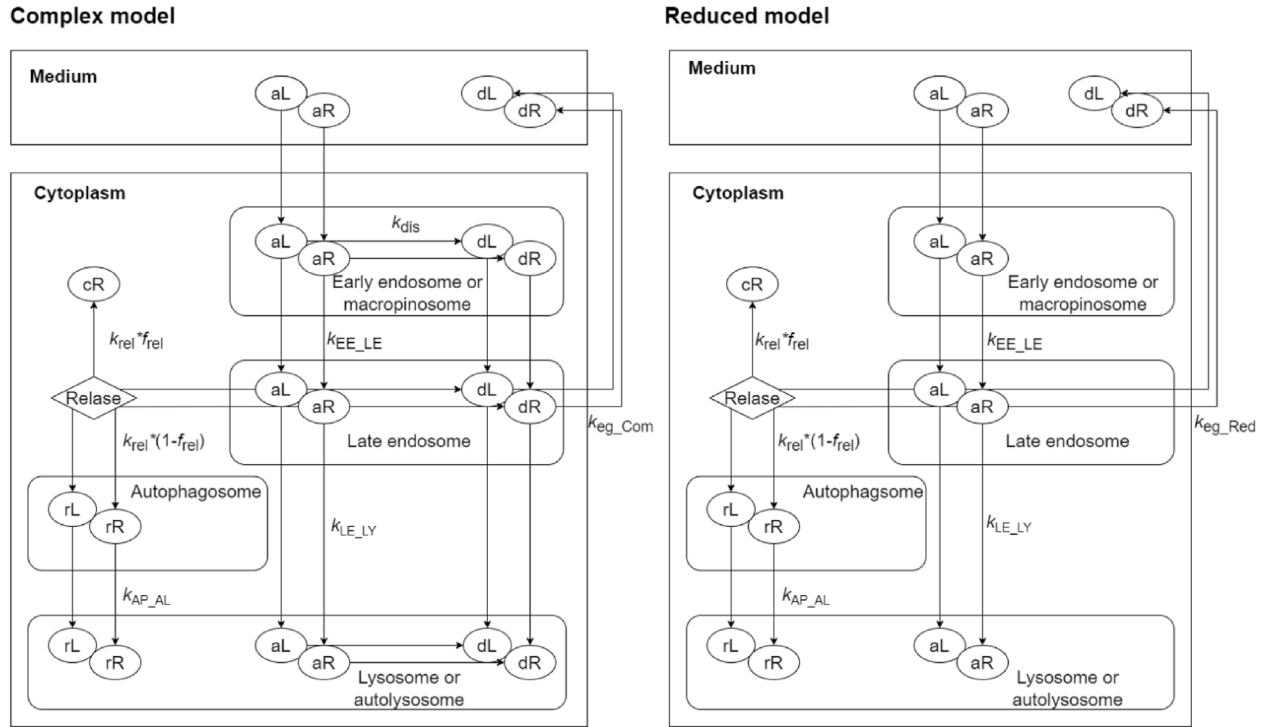
Figure 3 The PBPK model structure of LNP transportation in cells. First, the LNP with associated lipids (aL) and RNA (aR) is put in the culture medium. Then the LNP is taken up by cells and transferred *via* endosomes, in which LNP disassembly, RNA release, and egress of LNP take place[8,9,17]. The left panel is the complex model that is most mechanical. The right panel is a reduced model in which the process of LNP disassembly is not specifically simulated. aL and aR, lipids and RNA associated in LNP; dL and dR, lipids and RNA disassociated from LNP; cR, RNA really released to the cytoplasm; rL and rR, lipids and RNA wrapped in autophagosomes after release event taking place. k_{EE_LE}, transportation rate from early endosomes or macropinosomes to late endosomes; k_{LE_LY}, transportation rate from late endosomes to lysosomes; k_{dis}, LNP disassembly rate; k_{eg_Com}, egress rate in the complex model, k_{eg_Red}, egress rate in the reduced model; k_{rel}, RNA release rate; f_{rel}, the fraction of RNA released to the cytoplasm; k_{AP_AL}, transportation rate from autophagosomes to autolysosomes.

Lipid and RNA from the early to late endosomes:

$$\frac{dM_{EE\_LE}}{dt} = k_{EE\_LE} \cdot M_{EE} \tag{10}$$

Lipid and RNA from the late endosomes to lysosomes:

$$\frac{dM_{LE\_LY}}{dt} = k_{LE\_LY} \cdot M_{LE} \tag{11}$$

Free lipid and RNA dissociated from LNP:

$$\frac{dM_{intact\_free}}{dt} = k_{dis} \cdot M_{ass} \tag{12}$$

Egress of lipid and RNA:

$$\frac{dM_{LY-eg}}{dt} = k_{eg} \cdot M_{dis\_LE} \tag{13}$$

RNA released to the cytoplasm after the release event:

$$\frac{dM_{LY\_cyto}}{dt} = k_{rel} \cdot f_{rel} \cdot M_{ass\_LE} \tag{14}$$

RNA wrapped in autophagosomes after the release event:

$$\frac{dM_{LY\_AP\_RNA}}{dt} = k_{rel} \cdot (1 - f_{rel}) \cdot M_{ass\_RNA\_LE} \tag{15}$$

Lipid wrapped in autophagosomes after the release event:

$$\frac{dM_{LY\_AP\_lipid}}{dt} = k_{rel} \cdot M_{ass\_lip\_LE} \tag{16}$$

Lipid and RNA from autophagosomes to autolysosomes:

$$\frac{dM_{AP\_AL}}{dt} = k_{AP\_AL} \cdot M_{AP} \tag{17}$$

d*M*/d*t* (ng/h) is the mass change rate. *k* (1/h) is the kinetic rate. Subscripts of the symbols indicate the site, situation, or process experienced by the mass in discussion (EE, early endosome; LE, late endosome; LY, lysosome; AP, autophagosome; AL, autolysosome; "ass", assembled; "dis", disassociated; "lip", lipid; "eg", egress; "rel", release). In addition, k_{LE_LY} is assumed to be equal to k_{AP_AL}. The parameter f_{rel} (dimensionless) is the fraction of RNA released to the cytoplasm in relation to the RNA that undergoes the release event. Similarly, these change rates need to be combined into ODE for each compartment before simulation.

The cell model does not require physiological parameters such as the total volume or number of cells in the culture medium. The reason is that (1) their influence on LNP uptake was compensated for by constructing absorption profiles the same as the data; and (2) the subsequent transportation in cells was proportional to LNP taken up through modeling in the first-order kinetic manner, which is independent of cell numbers.

2.2.3. *Model fitting and simulation*
Before comparing critical parameters like k_{rel} and f_{rel} related to the RNA release ability of LNP formulations, some physiological parameters related to transfer between endosomes and LNP egress needed to be determined. Therefore, the first step of the work is to

simultaneously fit the model to the data of C12-200 and MC3 to calculate physiological parameters and specific pharmaceutical parameters. Then, specific parameters for L319 were fitted.

In the modeling work, substances that underwent the release event or disassembly were all deemed in the dissociated state (*e.g.*, cR, rR, and dR in Fig. 3); the total fraction of cR and rR based on all RNA in cells indicates the fraction of vesicles undergoing the release event; the fraction of cR and rR to all RNA in the modeling system at the end of simulation indicate the probability of RNA undergoing the release event.

In the fitting, the default "Isqnonlin" method was also used to estimate parameters. Error models were compared, and the best performance model was selected.

2.3. Molecular docking of ionizable lipids

Ionizable lipids are proposed to be metabolized by esterase. In order to characterize the binding affinity of ionizable lipids to the enzyme, Autodock Vina 1.1.2 (The Scripps Research Institute, La Jolla, CA, USA) was used to perform the molecular docking[27,28]. The crystal structure (PDB 2DQZ) of human carboxylesterase 1 (hCE1) was chosen as the macromolecule. The docking site was near the active site, the Ser221, Glu354, and His468 of the C chain[29,30]. The docking box center was $X = 45.089$, $Y = -5.945$, $Z = 62.349$. The docking box size was $X = 24.75$, $Y = 33.75$, and $Z = 29.25$. The macromolecule was rigid, while ionizable lipid molecules were flexible. The number of modes for each docking task was 50. The binding affinity of each mode was calculated automatically.

2.4. QM modeling of ionizable lipid metabolism

The hydrolysis of ester bonds by esterase can be divided into four steps (Supporting Information Fig. S3); however, the first step, in which the hydroxyl group of serine attacks the carbonyl carbon of the substrate to form the first intermediate (Td1), has been reported to be the rate-limiting step in many situations. Therefore, the calculation was focusing on this step[31-34].

The model was built using the cluster approach, that is, investigating the reaction profile in the active center with actual structure while the other part of the enzyme is reduced to a polarizable surrounding and kept fixed[35]. The cluster approach for esterase has been reported before[36,37]. The active site is recognized as an oxyanion hole and the serine-histidine-glutamate catalytic triad comes from the esterase[29,30]. In this study, the cluster approach was with the following structure[36]: methanol, imidazole, and formate anion indicate serine, histidine, and glutamate respectively, as well as two water molecules representing the oxyanion hole (Fig. 1).

Ionizable lipids are relatively large molecules for the QM method, as a result, the transition state of the reaction and the activation energy was difficult to determine. However, the Bell-Evans-Polanyi principle proves that activation energy is proportional to the energy change between reactions. Therefore, this study calculated the energy change between the T_d1 and the initial enzyme-substrate complex as a surrogate of biodegradability for the three ionizable lipids.

The first step is to determine the initial conformation of ionizable lipid molecules. To do that, a low-energy conformation ensemble was generated to sample favorable molecule conformer[38]. Herein, we carried out extended tight-binding quantum chemistry[39] (xtb), a molecular dynamics and quantum chemistry software package that keeps a balance between speed and accuracy, for conformational searching and initial geometry optimization, as well as Gaussian 16 (Gaussian, Inc., Wallingford, CT, USA) for further computation. Thousands of conformers were generated by the molecular dynamics function of xtb[40]. These conformers were then pre-optimized at semi-empirical GFN0-xTB level, followed by GFN2-xTB level under implicit aqueous solution model[41]. The top ten lowest-energy conformers in the last step were calculated under the density functional theory (DFT) level using Gaussian 16 (Gaussian, Inc.) to gain an accurate enough ranking and find out the real lowest-energy conformer. Geometry optimization and frequency correction were conducted under B3LYP[42]/6-31G(d) model chemistry plus D3 dispersion correction[43]. Single point energy was calculated under a more precise M06-2X[44]/6-31+g(d) level. In terms of the solvation model, the one used for geometry optimization and frequency calculation was IEFPCM[45] to prevent oscillation while SMD[46] model was used for single-point energy computation. The scaling factor for zero-point energy was 0.9806 according to the previous guideline[47]. Gibbs free energy was computed on Shermo software package[48]. Boltzmann's distribution of each conformer was calculated using Molclus software package. The calculation steps above were all under the temperature of 298 k (room temperature).

After successfully locating the side chain conformation of ester-containing lipids, it was adjusted to two complex minima of the first enzyme-catalyzed reaction: the T_d1 and the initial enzyme-substrate complex. Then their conformation underwent geometry optimization and Gibbs free energy calculation with the same manipulation stated above. Their relative energy gap was finally derived quantitatively to compare reaction rates.

3. Results and discussion

3.1. PBPK modeling on in vivo disposition of RNA-LNP

3.1.1. Model structure optimization

The model structure is the core of modeling. Since there was no standard model for RNA-LNP formulation before, the optimal model structure (Fig. 2) was determined by comparing the results of a series of structures fitted to the same rat PK data[13,25], and the result is shown in Fig. S2. The first two models were simple in structure and could not capture the PK curves (Fig. S2A and S2B). Then the model that is reported to be applied to multiple nano drugs[49] was referred to, however, an overestimation of lipid concentration in livers was observed (Fig. S2C). To address this overestimation issue and to interpret the uptake of LNP in various organs more mechanistically, one type of receptor was assumed to be distributed in the liver and spleen, and its concentration impacts the uptake rate. Some reasons contributed to this modification. First, for multiple ionizable lipids, including MC3, Lipid 5, and L319-like lipids, their LNPs were reported to primarily rely on the low-density lipoprotein receptor (LDLR) to be taken up by cells[7,13,50], and SM-102 is very similar to Lipid 5 (Fig. S1). Second, receptor concentration should be a factor that influences the uptake rate of LNP.

The change led to the optimal model structure and improved the fitting result (Fig. S2D). Some further modification was also considered, like adding a digestion tract compartment and building the digestion tract and the "other" organs the same as the liver and spleen in organ structure. However, it did not improve the fitting performance (Fig. S2E). Although the simulated PK curves are also close to the observed data, the higher AIC and BIC and

lower Log-likelihood proved that the modification was superfluous.

3.1.2.   Disposition of mRNA-LNPs with different ionizable lipids in rats

Ionizable lipid is the most important ingredient in LNP. Its ability of conditional being charged enables LNP to entrap RNA during manufacturing[24,51], adsorb plasma protein normally for cellular uptake[7,14], and release RNA when wrapped in endosomes[52]. The related critical processes were believed to be cellular uptake, disassembly, and metabolism in the liver and spleen, the two main target organs of LNP[14]. Cellular uptake relies on recognition between absorbed plasma proteins and receptors on cells and the type of protein absorbed shows selectivity to ionizable lipids[7]. LNP disassembly is related to RNA release and lipid metabolism. RNA release requires the interaction of lipids from LNP and endosomal membranes to form a non-bilayer lipid structure[52,53], which must disintegrate the LNP. Lipid metabolism is premised on LNP disassembly, as only single molecules can be catalyzed by enzymes. MC3, SM-102, and Lipid 5 all contain ester linkers and should be hydrolyzed by esterase[10]. Biodegradability is a concern of LNP[13,24]. Rapid metabolism of ionizable lipids allows for higher tolerance and more frequent dosages. As reported, the evolution of ionizable lipids from cationic lipids was partly due to the less toxicity[54,55], and the faster biodegraded SM-102 induces fewer adverse effects than the slowly biodegraded MC3[24].

Therefore, the first application of the model was to investigate the influence of ionizable lipids on the rate values of the three processes. The rat PK data of three mRNA-LNPs containing MC3, SM-102, and Lipid 5 as ionizable lipids was fitted[13,25]. For the three critical processes, scaling factors based on the rates of MC3 were designed to better describe the influence of ionizable lipids themselves on their PK behaviors. For the three LNPs, their permeabilities between the blood and interstitium in the liver and spleen were assumed to be the same in the first place. The reason is that these LNPs have similar sizes (80−100 nm), apparent pKa (6.30−6.68)[13], and zeta potential (−3.53−−3.88 mV)[25], and these hydrodynamic factors should dominate the penetration of big particles[56,57] through fenestrated sinusoidal capillaries in livers and spleens. Permeation also takes place in "other" organs. However, the endothelial vessel structure in other organs is different from livers and spleens, and the "other" compartment was just designed to balance the mass change in the whole body[49]. Therefore, no special control was conducted for parameters related to the "other" compartment.

The fitting result and parameters obtained are shown in Fig. 4A. The fitting result is pretty well for three types of ionizable lipids since the simulated PK profiles nearly overlap the observed data. The parameters obtained by fitting are also presented in Fig. 4A. The parameters k_{in} (uptake rate), k_{dis} (disassembly rate), and k_{el} (metabolism rate) in the liver and spleen first fitted for MC3 were kept fixed, and then the scaling factors of them for SM-102 and Lipid 5 were fitted respectively.

The results indicate that compared to LNP composed of MC3, those containing SM-102 or Lipid 5 have slower uptake rates (around 0.3- and 0.1-fold, respectively), higher disassembly rates (around 85- and 137-fold, respectively), and slightly higher (around 1.1- and 3.0-fold, respectively). The difference in uptake and disassembly rates between MC3 and Lipid 5 is consistent with the result from a cell assay[13], wherein MC3 induced more uptake of intact LNPs in cells but less release of mRNA in the cytoplasm. The structure of SM-102 is like Lipid 5. Thus, its slower uptake

but faster disassembly of LNP is reasonable. Surprisingly, although the PK profiles show large differences in the tissue lipid concentrations for three types of ionizable lipids, especially at the late phase of profiles, their metabolism rates just show small differences (less than 3-fold). Their huge difference in metabolism is first controlled by the upstream limiting step, the LNP disassembly process. It should be noted that changing the metabolism rates to a higher value for SM-102 and Lipid 5 manually might also induce an acceptable simulation since the lipid concentration at the late phase gets minimal. However, the significance of this modeling is that the metabolism rate of a lipid is not necessarily very high to achieve quick biodegradation and low toxicity. Disassembly is the priority to be considered. The parameter sensitivity analysis (PSA) in Supporting Information Fig. S4 also shows the disassembly rate has a greater influence on PK profiles than the metabolism rate.
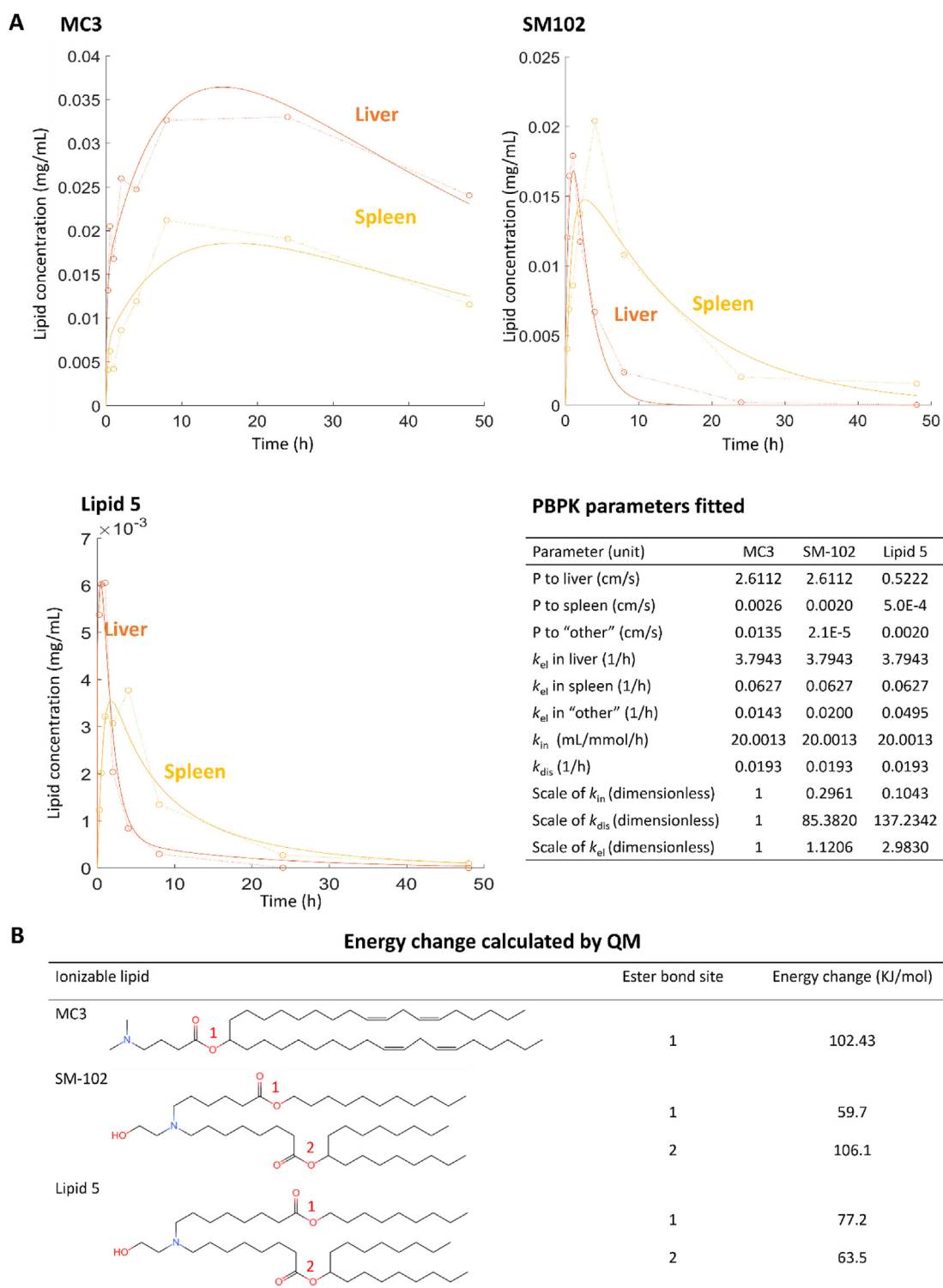
In the first place, the permeability in the liver and spleen was assumed to be the same for three types of mRNA-LNPs due to their similarity in pKa and particle size. However, this assumption was proven to be improper during the fitting work. The permeability rate of MC3 applies to SM-102, but that of Lipid 5 had to be down-regulated to get a satisfactory fitting. The underlying mechanism is unknown so far. Ionizable lipid is truly reported to influence the distribution of LNP, but this was concluded based on either ionizable lipids are obviously varied in carbon chain lengths[58], heads, or linkers[59], or formulations are varied in the molar ratio[60], or contain more than one charged lipids[61]. The difference between SM-102 and Lipid 5 is just the location of one ester linker. Its influence on the permeability of LNP needs to be further investigated. An interesting finding from the PSA (Fig. S4) is that the permeability shows a minimal influence on the liver PK profile, but the spleen PK profile is very sensitive to the change of permeability.

Based on an assumed receptor concentration in the liver, the scaling factor of receptor concentration in the spleen was fitted as around 0.37 (Table 1). The design of the scaling factor was due to limited resources reporting receptor (LDLR in this case) concentrations in organs. The fitted difference value is supported by mRNA copies of the gene in the public database. The RNA-seq data (https://www.ncbi.nlm.nih.gov/gene/300438) shows the LDLR expression level in livers is around six times higher than that in spleens for rats.

The biodegradation of the three ionizable lipids relies on the hydrolysis of their ester bonds catalyzed by esterase. To capture the biodegradation process well at a molecular level, we first conducted molecular docking between the lipid molecules and an esterase and then performed QM modeling. The docking work was to determine the strength of binding between substrates and the enzyme. The hCE1 was chosen as the enzyme because: (1) this enzyme is found to form a complex with and catalyze the hydrolysis of a long molecule, palmityl CoA[30]; (2) this enzyme is abundant in livers; (3) this enzyme is inter-species conserved[62]. However, the binding affinity of the three ionizable lipids is similar, around −6.1 kcal/mol (Supporting Information Fig. S5) which indicates that the difference in biodegradability of the three lipids is not attributed to the binding process.

The QM modeling was used to calculate the energy gap in hydrolysis to estimate the biodegradability of lipids. QM is a precise calculation method but costs a lot of computational power. Therefore, the cluster approach was adopted which only considers a limited number of atoms around the active site at a quantum mechanical level. Our cluster approach referred to a previously

PBPK parameters fitted

Parameter (unit)	MC3	SM-102	Lipid 5
P to liver (cm/s)	2.6112	2.6112	0.5222
P to spleen (cm/s)	0.0026	0.0020	5.0E-4
P to "other" (cm/s)	0.0135	2.1E-5	0.0020
k_{el} in liver (1/h)	3.7943	3.7943	3.7943
k_{el} in spleen (1/h)	0.0627	0.0627	0.0627
k_{el} in "other" (1/h)	0.0143	0.0200	0.0495
k_{in} (mL/mmol/h)	20.0013	20.0013	20.0013
k_{dis} (1/h)	0.0193	0.0193	0.0193
Scale of k_{in} (dimensionless)	1	0.2961	0.1043
Scale of k_{dis} (dimensionless)	1	85.3820	137.2342
Scale of k_{el} (dimensionless)	1	1.1206	2.9830

Energy change calculated by QM

Ionizable lipid	Ester bond site	Energy change (KJ/mol)
MC3	1	102.43
SM-102	1	59.7
	2	106.1
Lipid 5	1	77.2
	2	63.5

Figure 4 Modeling result of rats' PK and biodegradability of ionizable lipids. (A) Rats received intravenous administration of mRNA-LNP containing different ionizable lipids (MC3, SM-102, Lipid 5) at the dose of 0.2 mg/kg mRNA (equivalent to about 2.23 mg/kg for MC3, and 2.46 mg/kg for SM-102 and Lipid 5). The mean concentration of ionizable lipids at different time points (the dots) was extracted from the original study[13,25]. The *in vivo* PBPK model was fitted to the original data, resulting in optimized PK curves (the solid lines) and parameter values. (B) QM calculation of the energy change between the initial reaction complex and the first tetrahedral intermediate during esterase catalyzation using the cluster approach.

reported setting dealing with ester bond hydrolysis[36]. This is reasonable since the esterase family has highly conserved structures, sharing the common active site of the same core catalytic mechanism[37,63]. Since it is difficult to determine the precise transition state energy for the three lipids due to their big sizes, the energy change in the first step of the hydrolysis reaction (Fig. S3) was calculated as a surrogate of biodegradability according to the Bell-Evans-Polanyi principle. This principle is based on a phenomenon that 'for a series of homologous chemical reactions, a more endothermic (exothermic) reaction leads to a higher (lower) energy gap'. Some previous studies[64,65] adopted the Bell−Evans−Polanyi principle to compare reaction rates indirectly, avoiding locating transition state structure.

The QM result is shown in Fig. 4B. MC3 has only one ester bond with an energy change of over 100 kJ/mol. SM-102 has two ester bonds, and the energy change at Site 1 is 59.7 kJ/mol, making this bond the main target of catalysis. Thus, SM-102 is more likely to be metabolized than MC3. Lipid 5 has two ester bonds with an energy change of around 70 kJ/mol, making it also more likely to be metabolized than MC3. This result is consistent with that calculated from PBPK. However, because the action energy has not been determined yet, the precise kinetic rate cannot be calculated from QM at this time and compared to the PBPK result.

3.1.3. Transportation of siRNA-LNPs with different particle sizes in mice

Then, the PBPK model was used to characterize LNPs with different sizes. The effect of size was investigated in mice using siRNA-LNP. The model for siRNA is the same as mRNA because we only focused on processes related to RNA transfer other than those of RNA exerting effects, and the transfer routes for both RNA are the same until the RNA is released from endosomes. Besides, both formulations are similar in their LNP composition and ratio of lipid to RNA.

First, LNP at the diameter of 80 nm containing MC3 was modeled. In the original study[16], PK data of intravenous administration at the 0.03, 0.3, and 1 mg/kg siRNA (equivalent to 0.33, 3, 11.1 mg/kg of lipid) was presented. They showed similar time courses of percent dose remaining in blood, liver, and plasma, implying a linear relationship between dose and exposure, which was also supported by many other animal test results[26]. Besides, the study traced the distribution of LNP to organs with 3H-CHE labeling, a marker that is non-exchangeable and non-metabolizable[66]. Summarizing this information, the PK result calculated based on 11.1 mg/kg of lipid injection was decided to be fitted. The result should be general due to the linear relationship. Besides, in the model, processes of LNP disassembly and metabolism in the liver and spleen were shut off, but the elimination route in "other" was maintained to trap superfluous lipids. The fitting result and parameters obtained are shown in Fig. 5A, with the scaling factor of receptor concentration between the liver and spleen fitted to be 0.1217 (Table 1).

Compared to the parameters of MC3 for rats, the permeability to the liver in mice is higher, while the permeability to the spleen is lower. This contradicts what can be plainly read from the mice PK result wherein the lipid concentration in the liver is lower than that in the spleen. However, this can be explained by their difference in physiological parameters. Mice have a relatively smaller endothelial surface area in the liver but a larger area in the spleen (Table 1) which asked for corresponding changes in permeabilities to compensate for this difference. Other physiological parameters like organ volumes and blood flow all made their contributions to the PK results. Besides, the receptor in organs also impacts LNP distribution. Similar to rats, the scaling factor fitted indicates that the receptor concentration in the liver is larger than that in the spleen for mice, which is also supported by an LDLR RNA-seq result (https://www.ncbi.nlm.nih.gov/gene/16835). This indicates that the parameters fitted match the physiological condition of mice and allow formulations to be compared in them.

Then, LNP at diameters of 78 and 45 nm was modeled. In the original study[14], the mice were intravenously administered with FVII siRNA at 0.3 mg/kg (equivalent to the ionizable lipid DMAP-DLP (Fig. S1) at about 3.42 mg/kg) and ^{3}H-CHE labeling was also used to trace the organ distribution. Since the ionizable lipid they contain is similar to MC3, therefore parameters determined in Fig. 5A were first tried to simulate the PK of the 78 nm LNP and the result is shown in Supporting Information Fig. S6. The PK curves of lipids in blood and liver were very accurate, while lipids in the spleen were within a 1.5-fold error of the experimental data. Then, parameters were further optimized by fitting.

For the 78 nm LNP containing DMAP-DLP, the permeability and uptake rate of MC3-LNP are suitable (Fig. 5B). The gap in the permeability of spleens may be due to the difference in their molecular properties. Compared to the LNP at 78 nm, the LNP at 45 nm shows less permeability to the liver but a much higher uptake rate (Fig. 5C). The high uptake rate is understandable from the high corner appearing in the PK curve of the 45 nm particle taken up in the liver, which is a sign that the LNP is rapidly and irreversibly absorbed into the liver, and this is dominated by the uptake of LNP from interstitium to cells. In such a case, the contribution of permeability to absorption may become concealed. Overall, the fitting result is satisfactory.

However, a previous interesting finding is that LNP at the size of 45 nm was taken up by livers much faster than LNP of 78 nm but showed less ability in knocking down genes[14]. The authors compared the disassociation rate of ionizable lipids from LNPs with the two particle sizes and supposed that the 45 nm LNP disintegrating more quickly conveyed less ionizable lipids into livers leading to compromised knockdown ability. Subsequently, the authors used 30 nm LNPs at different N/P ratios proving that a higher ratio of ionizable lipids could improve the knockdown ability.

However, since the experiment did not directly show the ionizable lipid concentration in livers for the 45 and 78 nm LNP, we performed a simulation on the concentration further considering lipid dissociation. Based on the model shutting off LNP disassembly and metabolism, ionizable lipid disassociation processes were added to LNP in all blood and interstitium compartments, with the disassociation rates (k_{dis_plasma}) fitted through a one-compartmental PK model (Fig. 6A). Then the same situations (as Fig. 5B and C) were simulated to calculate ionizable lipid concentration in livers (Fig. 6B). The result shows the LNP at 45 nm still carries more ionizable lipids into the liver than that at 78 nm, even when lipid disassociation is considered. Therefore, there must be other factors contributing to the better knockdown ability of LNP at 78 nm. Further investigation about it may involve the tool of the PBPK model simulating RNA release which is discussed later.
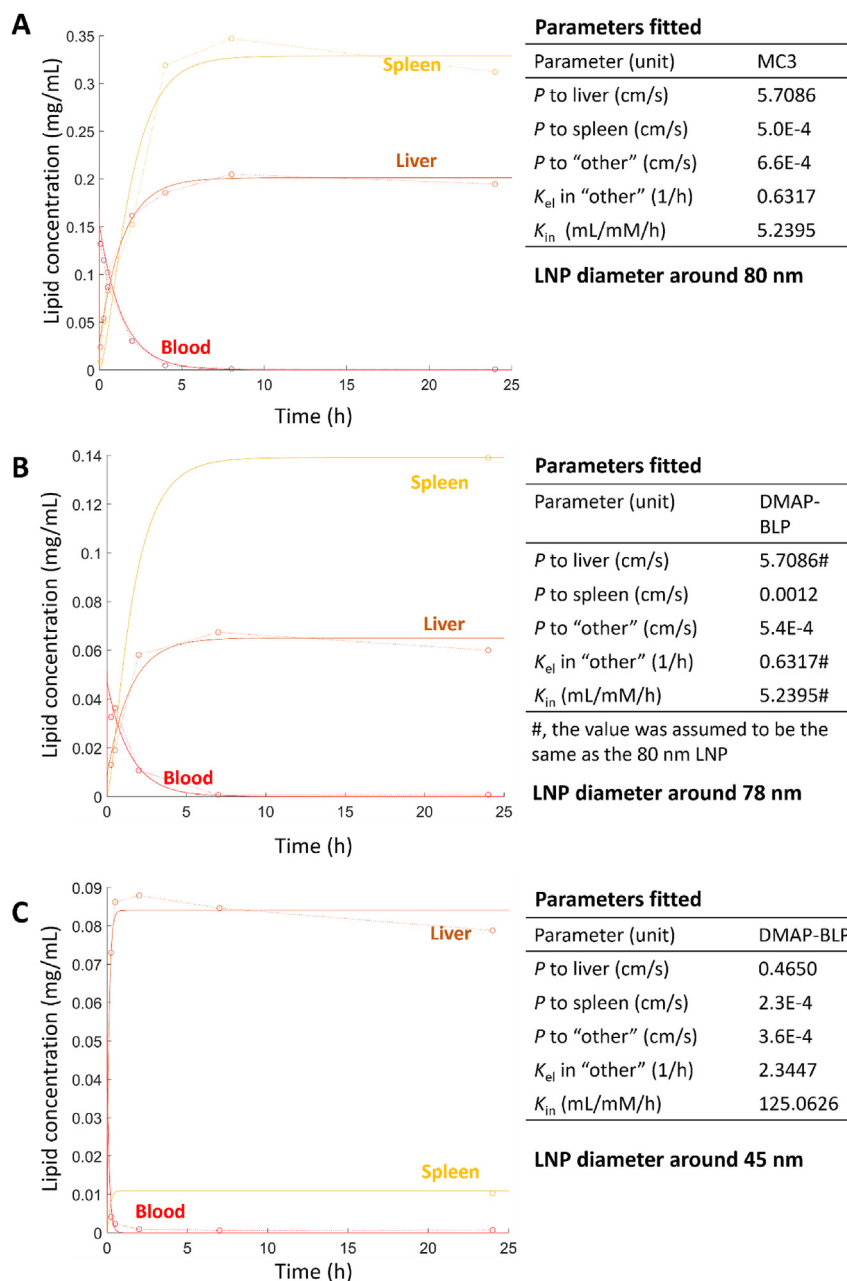
Figure 5 PBPK model fitting results of siRNA-LNP in mice and parameters fitted. (A) Mice were intravenously administered with siRNA-LNP at the lipid dose of 11.1 mg/kg. LNP was composed of MC3 as the ionizable lipid and at a particle size of around 80 nm[16]. (B and C) Mice were intravenously administered with siRNA-LNP at the 0.3 mg/kg siRNA (equivalent to about 3.42 mg/kg DMAP-DLP). LNP was at the size of around 78 and 45 nm, respectively[14]. The mean concentrations of ionizable lipids at different time points (the dots) were calculated based on the signal of 3H-CHE labeled on LNP in the original study. The *in vivo* PBPK model, which excludes the disassembly and metabolism processes, was fitted to the original data, resulting in optimized PK curves (the solid lines) and parameter values.

3.1.4. *Transportation of siRNA-LNPs at different doses treated in humans*

PBPK is becoming an important tool in clinical. For example, PBPK can be used to estimate the dose used in the first-in-human study[67] and in individualized regimens[68]. Therefore, an attempt was made to generalize our PBPK model to human data.

Patisiran (Onpattro®) is the first approved siRNA-LNP formulation in which MC3 is used. The review document of the drug includes the PK data of healthy volunteers (clinical trials

ALN-TTR02-001 and ALN-TTR02-005) which is desired for our usage. In the first place, parameters fitted from mice PK data were attempted to be used in combination with human physiological parameters (Table 1) to capture the PK profiles in humans. However, the simulated plasma MC3 concentration was much less than the observation. Thus, fitting is necessary. To consider the issue of model solvability, the model structure was further reduced by shutting off the permeation to the spleen and elimination in the "other" organ.
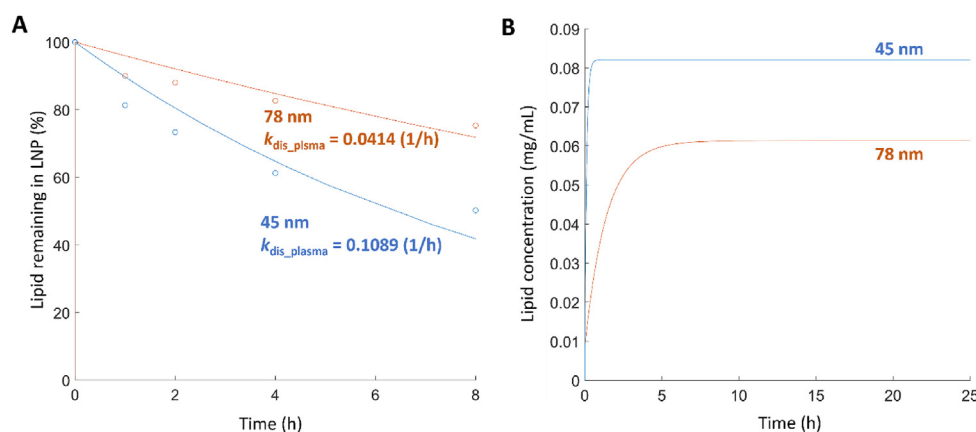
Figure 6 Ionizable lipid disassociation from LNPs and mice hepatic ionizable lipid concentration simulation considering dissociation. (A) LNPs at 45 or 80 nm were incubated in mice plasma *in vitro*, and the ionizable lipid fractions remaining in LNP at different time points were reported (the dots)[14]. A one-compartmental PK model was fitted to the data, resulting in the optimized remaining lipid curves (the solid lines) and disassociation rates ($k_{\text{dis\_plasma}}$). (B) Based on the model and parameters in Fig. 5B and C, the same cases were simulated to calculate mice hepatic ionizable lipid concentration by further considering its dissociation from LNP in plasma and interstitium.

With the resulting model, the PK data of 0.5 mg/kg patisiran was first fitted and parameters were obtained (Fig. 7). After that, the parameters were fixed, and the PK for other doses was simulated. As the results show, the fitting and simulation are with good accuracy. The simulation overlaps with the observed result for at least up to 1000 h (more than 41 days). Therefore, the model is applicable to the simulation of various doses. Besides, one advantage of PBPK modeling is to combine pharmaceutical properties with altering physiological conditions of populations to predict the PK in them[69].

However, it cannot be denied that applications of the current PBPK model are limited. In fact, this model cannot provide much more information than the already developed population PK
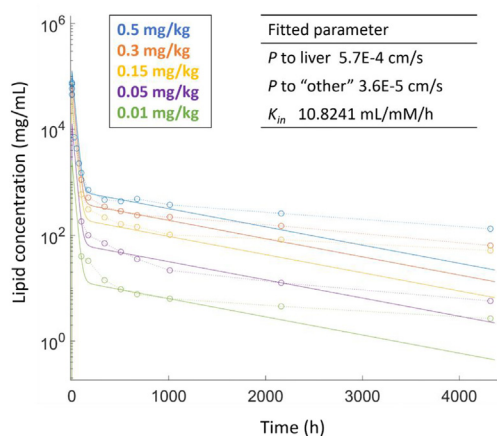

Figure 7 PBPK model fitting result of human PK data of siRNA-LNP at different doses. Healthy human subjects intravenously received patisiran at the dose of 0.01, 0.05, 0.15, 0.3, and 0.5 mg/kg (phase 1 clinical trials ALN-TTR02-001 and ALN-TTR02-005). The mean concentration of ionizable lipids MC3 at different time points (the dots) was extracted from the original study[26]. The reduced *in vivo* PBPK model was fitted to the data of 0.5 mg/kg, resulting optimized PK curve (the blue solid line) and parameter values. Then, these parameters were fixed, and other doses were simulated (the other solid lines).

model of patisiran[26]. Developing a more refined model is urgently needed in this field[70,71]. One of the potential improvements is to incorporate the mechanisms related to LNP delivery into models. Thus, a PBPK model simulating the LNP transportation in cells was built as an exploration in this field.

3.2. PBPK modeling on cellular transportation of siRNA-LNP

3.2.1. Characterizing physiologically related parameters
The Hela cell is a very commonly used tool to investigate the delivery and pharmacology of LNP. siRNA-loaded LNP transportation in the cell has been deeply researched in previous studies[8,9,17]. The authors used confocal microscopy or electron microscopy to find the co-localization of LNPs and various cellular vesicles or critical proteins to identify their experience, which can be summarized as the model structure shown in Fig. 3. Compared to the model structures reported in previous studies[21,72,73], our built model highlights both the transportation of lipid and RNA components considering the processes of uptake and egress of LNP, and specifically calculates the fractions of RNA which is just undergoing the release event or is truly released to cytoplasm.

The goal of modeling is to identify the factors from LNP itself contributing to its performance. To do that, rates of physiological processes, such as LNP transportation between different vesicles and the egress of LNP, had to be discriminated. In the research of C12-200, cellular LNP uptake, disassembly, and egress were investigated[9]. Specifically, the cell was incubated with LNP for 3 h, and then was washed to monitor the LNP egress for 25 h. In the research of MC3, time courses of LNP uptake, LNP fractions in early- and late-endosomes, and lysosomes were tested for up to 6 h[17]. To combine the two datasets, the cellular PBPK model was fitted to them simultaneously. The C12-200 was fitted with both model structures, while the MC3 was just fitted with the reduced model due to the data limit. All models shared the transfer rate of LNP between cellular vesicles, the two fittings of C12-200 used the same release rate, and the two fittings based on the reduced model structure shared the same LNP egress rate. With these settings, the fittings were linked together, and the result is shown in Fig. 8.

Fig. 8 shows the fitting was generally satisfactory (mean squared error is 0.0232). Fig. 8C shows the parameters fitted, including physiological parameters controlling LNP transfer in the cell and egress and pharmaceutical parameters specific to C12-200. The release rate, k_{rel}, of C12-200 could be fitted in this case because the cR, rR, and dR (Fig. 3) were all deemed in the disassociated status, which is supported by the molecular simulation result[74].

3.2.2. Comparison in pharmaceutically related parameters among three ionizable lipids formulated in LNPs
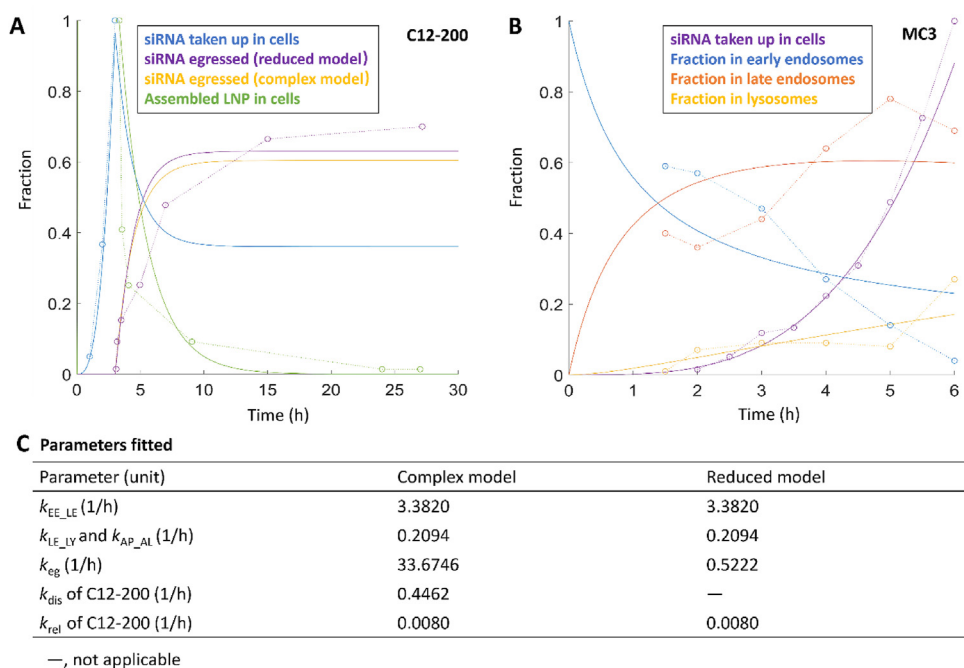
Based on physiological parameters obtained before, the release behavior of other LNPs can be fitting. The index of the fraction of vesicles undergoing the release event referred to the result of siRNA released from L319-based LNP in cells[8]. The authors found that when an endosome containing LNP experiences the release of siRNA, the damaged endosome recruits the protein galectin-8, which consequently leads it to be engulfed by autophagosomes. The test showed that only around 7% of cellular vesicles containing LNPs were co-localized with galectin-8, which meant only 7% of internalized siRNA underwent the release event. Besides, only half of siRNA could eventually escape into the cytoplasm ($f_{rel} = 0.5$) even if the release event happens to an endosome, which was evidenced by the detected fluorescence signal.

This series of information, along with the given cellular uptake data (Fig. 9A) and the physiological parameters fitted above, allowed the parameterization of the critical release rate (k_{rel}) of L319-LNP, which was 0.0157 (Fig. 9B and D). Note that the

steady state was achieved by extending the simulation time due to no metabolism route was included in the model. After that, the fraction of cR and rR (Fig. 3) to all siRNA in the model was simulated as the probability of siRNA undergoing the release event, which was slightly over 0.021. Surprisingly, a similar probability could be calculated from the cell test[8]. In the test, siRNA targeting eGFP was delivered via L319-LNP into eGFP-expressing cells. At the end of the test, the fluorescence signal of the cells decreased to around 0.1-fold to the initial value, and the number of LNPs each cell took up was more than 100. Besides, the eGFP knockdown of a single cell was identified as an "all-or-nothing" event, which means the siRNA release of merely one LNP was enough to extinguish the fluorescence signal of the cell. Therefore, if the release event of a single LNP is considered as a Bernoulli experiment with a certain probability p, and if the probability that all 100 repetitions of the Bernoulli's test result in a negative outcome is 0.1, then p can be calculated to be approximately 0.0228 using Eq. (18). This value is close to the probability of 0.021 that was derived via simulation.

$$(1-p)^{100} = 0.1 \tag{18}$$

For the situation of MC3, the fraction of siRNA released to the cytoplasm based on all cellular siRNA was measured as 0.0134, but the measurement of f_{rel} was not reported[17]. However, since the MC3 is like L319 in structure (Fig. S1) assuming the f_{rel} of MC3 as 0.5, equivalent to that of L319, was reasonable. Combining this information with the uptake profile of MC3 (Fig. 8B) the release rate was fitted as 0.0058 (Fig. 9D) and the probability of siRNA undergoing the release event was also simulated (Fig. 9C).

C Parameters fitted

Parameter (unit)	Complex model	Reduced model
k_{EE_LE} (1/h)	3.3820	3.3820
k_{LE_LY} and k_{AP_AL} (1/h)	0.2094	0.2094
k_{eg} (1/h)	33.6746	0.5222
k_{dis} of C12-200 (1/h)	0.4462	—
k_{rel} of C12-200 (1/h)	0.0080	0.0080

—, not applicable

Figure 8 Fitting result of cellular transportation of the LNP containing C12-200 or MC3. (A) Hela cells were incubated with LNP containing C12-200 for 3 h and then washed to remove the medium. The data of LNP uptake up to 3 h and LNP disassembly, and exocytosis in the following 25 h were extracted from the original study[9] (the dots). (B) Hela cells were incubated with LNP containing MC3 for 6 h. The data of LNP uptake and fraction in early endosomes, late endosomes, and lysosomes were extracted from the original study[17] (the dots). The cellular PBPK model was fitted to data of C12-200 (with complex and reduced model structure) and MC3 (with reduced model structure) simultaneously, sharing values of rates of transfer from early endosomes to late endosomes (k_{EE_LE}) from late endosomes to lysosomes (k_{LE_LY}) from autophagosomes to autolysosomes (k_{AP_AL}) and egress out of cells (k_{eg}). The resulting optimized PK curves (the solid lines) were presented. (C) Parameters fitted to C12-200-LNP and physiological processes.
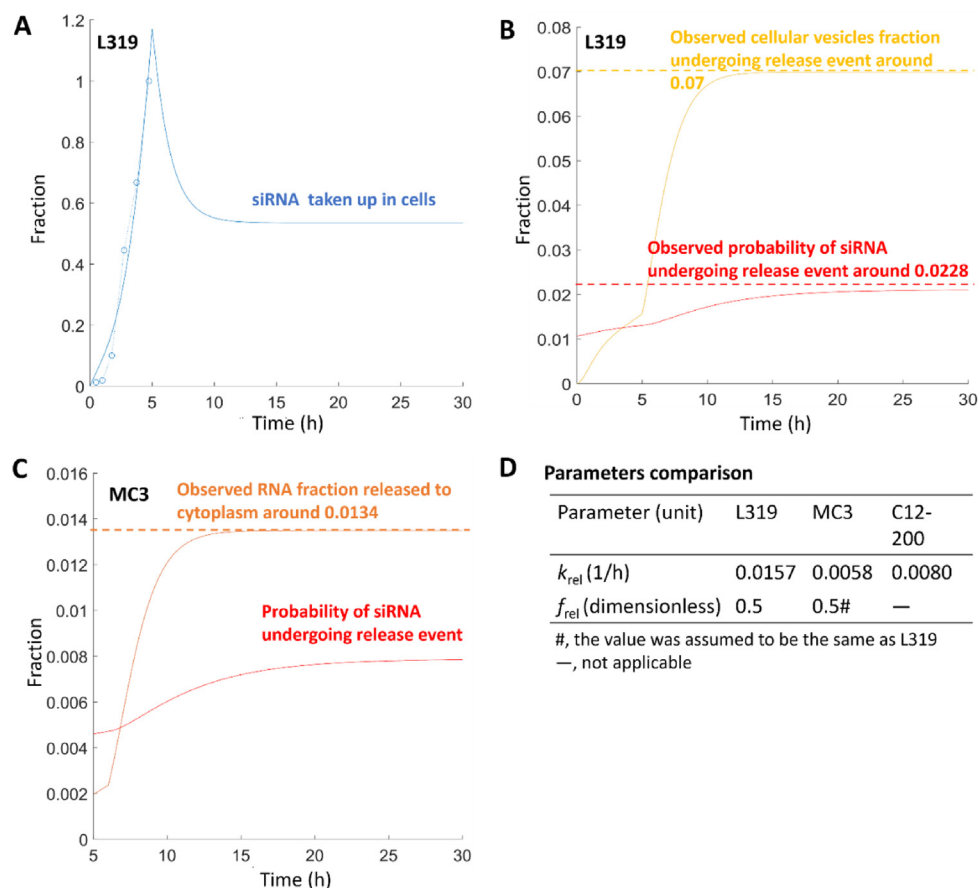
Figure 9 Fitting and simulation of cellular transportation of the LNP containing L319 and MC3. (A) The reduced cellular PBPK model was fitted to uptake data (the points) of LNP containing L319 incubated with Hela cells[8], obtaining the uptake profile (solid line). (B) The fraction of vesicles undergoing the release event for L319 was observed in the original study (the yellow dashed line). The sum of cR and rR based on all RNA in cells was fitted to the fraction (the yellow solid line) obtaining the RNA release rate (k_{rel}). Based on that, the probability of siRNA undergoing the release event, which is the fraction of cR and rR to all RNA in the modeling, was simulated (the red solid line) and compared to the experimental data (the red dashed line). (C) The fraction of RNA released to the cytoplasm for MC3 was observed in the original study[17] (the orange dashed line). The cR based on all RNA in cells was fitted to the fraction (the orange solid line) obtaining k_{rel} and the following simulated probability of siRNA undergoing the release event (the red solid line). (D) Comparison in critical parameters related to siRNA release of LNPs containing L319, MC3, and C12-200.

For the situation of C12-200, its k_{rel} was fitted as 0.0080 (Figs. 8C and 9D). Its f_{rel} could not be obtained since related results were not reported from the source literature[9], and the chemical structure of C12-200 is very different from other ionizable lipids.

Eventually, parameters representing the ability of RNA release of the LNPs of the three ionizable lipids were obtained. They are critical for RNA release, which is reflected by the PSA result of Supporting Information Fig. S7. Change of k_{rel} in the range between −0.2- to 5-fold of the original value results in release probability from 0.005 to 0.1. Compared to the pure results from the cell assays, these parameters discriminated from confounding physiological factors are more basic for drug formulations and useful for comparison between formulations. In the above PK simulation of LNPs at the size of 45 and 78 nm, we have suggested that the 78 nm LNP performs better than the 45 nm LNP in gene knockdown efficiency may be due to factors more than the mass of lipids entering livers. In fact, the size or curvature of the particle is one of the underlying factors influencing the performance of lipid-based formulations, such as the binding constants

between bio-molecules located at membranes[75] and the fusion of membranes[74]. We suppose the effect of size should be contained in the parameters since they characterize the interaction between lipid layers of LNP and endosomal membranes.

4. Assumptions in the model and perspectives

The present PBPK model is successfully built under some necessary assumptions (Supporting Information Table S1) and inevitably has some limitations. First, as the *in vivo* model shown in Fig. 2, the structure is simple relative to a whole-body model. Drug distribution into organs is considered at the liver and spleen. This is applicable to the three ionizable lipids, MC3, SM-102, and Lipid 5, but for other formulations which, for example, show improved distribution to the lung[76], the model needs improvements. Besides, the PK of patisiran shows there is a minimal secondary peak in the plasma MC3 concentration curve, suggesting a pump-out process from organs to blood[15]. But in animal data, this efflux effect is inconspicuous, therefore, this process was not added to the model.

Second, in the *in vivo* model, only one receptor type is involved with an assumed concentration. It is proper in our model because LDLR is the dominant receptor of the three types of LNPs. However, it should be noted that other types of proteins are also likely to mediate the internalization, and ionizable lipids show sensitivity to the protein type[7]. The parameters need to be adapted to specific conditions.

Third, the same value of permeability was applied to multiple conditions in the first place since it is assumed to be dependent on the particle size, apparent pKa, and zeta potential of LNP. This was enlightened by other modeling work for nanoparticles, wherein the *in vivo* behavior of particles can be derived from the physico-chemical properties[49]. However, our PBPK model does not directly link physicochemical properties to the *in vivo* parameters, which is an important issue to be further improved in future work.

Fourth, in the cellular PBPK model, RNA and lipids would not be re-taken up if emitted out from cells. In the original study, the fluorescent label on RNA was traced to unravel the trafficking of LNP in the cells. No method was applied to show the trace of lipid molecules and naked RNA is difficult to enter most types of cells[77]. Therefore, neglecting their reuptake is reasonable in this case. The process has not been investigated.

Fifth, in the cellular model, the simulation is terminated at the stage of lysosomes. The original data does not reflect the metabolism of RNA and/or lipids, as the measured signal was from the fluorescent label.

Another limitation is the empirical modeling of LNP uptake in the cellular model. The LNP internalization is really a complex process, which involves two interactive entry pathways, endocytosis, and macropinocytosis, under the control of multiple cellular proteins[9,17]. Modeling LNP uptake mechanistically is a challenging but interesting topic. More deep research is needed.

In terms of QM modeling, it is regretful that the absolute activation energy has not been investigated in this study. The calculation of activation energy depends on the identification of the transition state. However, ionizable lipids are large molecules, and it is challenging to observe their transition states. Without the activation energy, a precise kinetic rate of hydrolysis cannot be derived. However, the biodegradability of the three lipids has been roughly compared through the Bell-Evans-Polanyi principle. Besides, increasing the molecule numbers in the QM model or extending it to the quantum mechanics/molecular mechanics (QM/MM)[78] model to better mimic a real enzyme can be considered in the future.

Although there are some limitations, this QM/PBPK approach still has the potential to advance the research of nanomedicines. PBPK modeling has been applied to various types of nanoparticles, including gold, iron, polymeric, and liposome particles[79]. Through PBPK methods, a macroscopic picture of drug PK in bodies can be concentrated on some key parameters at a subscale level. The mechanistic details of these critical processes can be further unraveled in a microscopic picture by tools like QM modeling. This multi-level modeling approach[80,81] integrates the understanding of nanoparticles *in vivo*. The QM method is able to predict the properties such as biodegradability and safety of ingredients without prior experiments.

5. Summary

Our study successfully constructed multi-scale modeling of LNP, including PBPK models of RNA-LNP delivery in Hela cells, rats, mice, and humans, and QM modeling of the biodegradability of ionizable lipids. Key factors dominating the PK of LNP with different ionizable lipids, particle sizes, and doses were quantitatively characterized, which is helpful in predicting PK profiles in new conditions. We found that the LNP disassembly rate has a great influence on the metabolism of ionizable lipids. The hydrolysis of ionizable lipids was simulated by PBPK and QM methods, which showed consistent results. This finding supports the estimation of biodegradability and safety of the formulation. The cellular PBPK model determined a key parameter (release rate) as a good indicator of the interaction between LNP and endosomal membranes and can predict RNA release probability. In summary, new understandings of LNP transportation in bodies and cells are derived from the QM/PBPK modeling approach by integrating multiple source data. The findings and methodology have the potential to facilitate the rational design of ionizable lipids, RNA-LNP, and other nanomedicine formulations.

Author contributions

Defang Ouyang and Wei Wang designed the research. Wei Wang collected the data, conducted the PBPK modeling, molecular docking, and performed data analysis. Shiwei Deng conducted the QM modeling and performed data analysis. Wei Wang and Shiwei Deng wrote the manuscript. Defang Ouyang and Jinzhong Lin revised the manuscript. All of the authors have read and approved the final manuscript.

Conflicts of interest

The authors have no conflicts of interest to declare.

Appendix A.   Supporting information

Supporting information to this article can be found online at https://doi.org/10.1016/j.apsb.2024.06.011.

References

1. Ledford H. Gene-silencing technology gets first drug approval after 20-year wait. *Nature* 2018;**560**:291−2.
2. Tanne JH. Covid-19: Pfizer-BioNTech vaccine is rolled out in US. *BMJ* 2020;**371**:m4836.
3. Mahase E. Covid-19: UK approves Pfizer and BioNTech vaccine with rollout due to start next week. *BMJ* 2020;**371**:m4714.
4. Suzuki Y, Ishihara H. Difference in the lipid nanoparticle technology employed in three approved siRNA (Patisiran) and mRNA (COVID-19 vaccine) drugs. *Drug Metab Pharmacokinet* 2021;**41**:100424.

5. Hou X, Zaks T, Langer R, Dong Y. Lipid nanoparticles for mRNA delivery. *Nat Rev Mater* 2021;**6**:1078−94.

6. Hald Albertsen C, Kulkarni JA, Witzigmann D, Lind M, Petersson K, Simonsen JB. The role of lipid components in lipid nanoparticles for vaccines and gene therapy. *Adv Drug Deliv Rev* 2022;**188**:114416.

7. Miao L, Lin JQ, Huang YX, Li LX, Delcassian D, Ge Y, et al. Synergistic lipid compositions for albumin receptor mediated delivery of mRNA to the liver. *Nat Commun* 2020;**11**:2424.

8. Wittrup A, Ai A, Liu X, Hamar P, Trifonova R, Charisse K, et al. Visualizing lipid-formulated siRNA release from endosomes and target gene knockdown. *Nat Biotechnol* 2015;**33**:870−6.

9. Sahay G, Querbes W, Alabi C, Eltoukhy A, Sarkar S, Zurenko C, et al. Efficiency of siRNA delivery by lipid nanoparticles is limited by endocytic recycling. *Nat Biotechnol* 2013;**31**:653−8.

10. Maier MA, Jayaraman M, Matsuda S, Liu J, Barros S, Querbes W, et al. Biodegradable lipids enabling rapidly eliminated lipid nanoparticles for systemic delivery of RNAi therapeutics. *Mol Ther* 2013;**21**:1570−8.

11. Sun DX, Gao W, Hu HX, Zhou S. Why 90% of clinical drug development fails and how to improve it?. *Acta Pharm Sin B* 2022;**12**:3049−62.

12. Zhao L, Kim MJ, Zhang L, Lionberger R. Generating model integrated evidence for generic drug development and assessment. *Clin Pharmacol Ther* 2019;**105**:338−49.

13. Sabnis S, Kumarasinghe ES, Salerno T, Mihai C, Ketova T, Senn JJ, et al. A novel amino lipid series for mRNA delivery: improved endosomal escape and sustained pharmacology and safety in non-human primates. *Mol Ther* 2018;**26**:1509−19.

14. Chen S, Tam YYC, Lin PJC, Sung MMH, Tam YK, Cullis PR. Influence of particle size on the *in vivo* potency of lipid nanoparticle formulations of siRNA. *J Control Release* 2016;**235**:236−44.

15. Zhang XP, Goel V, Robbie GJ. Pharmacokinetics of patisiran, the first approved RNA interference therapy in patients with hereditary transthyretin-mediated amyloidosis. *J Clin Pharmacol* 2020;**60**:573−85.

16. Mui BL, Tam YK, Jayaraman M, Ansell SM, Du X, Tam YYC, et al. Influence of polyethylene glycol lipid desorption rates on pharmacokinetics and pharmacodynamics of siRNA lipid nanoparticles. *Mol Ther Nucleic Acids* 2013;**2**:e139.

17. Gilleron J, Querbes W, Zeigerer A, Borodovsky A, Marsico G, Schubert U, et al. Image-based analysis of lipid nanoparticle-mediated siRNA delivery, intracellular trafficking and endosomal escape. *Nat Biotechnol* 2013;**31**:638−46.

18. Jones HM, Rowland-Yeo K. Basic concepts in physiologically based pharmacokinetic modeling in drug discovery and development. *CPT Pharmacomet Syst Pharmacol* 2013;**2**:1−12.

19. Wang W, Ouyang DF. Opportunities and challenges of physiologically based pharmacokinetic modeling in drug delivery. *Drug Discov Today* 2022;**23**:2100−20.

20. Wu F, Shah H, Li M, Duan P, Zhao P, Suarez S, et al. Biopharmaceutics applications of physiologically based pharmacokinetic absorption modeling and simulation in regulatory submissions to the U.S. Food and Drug Administration for new drugs. *AAPS J* 2021;**23**:31.

21. Ayyar VS, Song DW, Zheng SM, Carpenter T, Heald DL. Minimal physiologically based pharmacokinetic-pharmacodynamic (mPBPK-PD) model of *N*-acetylgalactosamine−conjugated small interfering RNA disposition and gene silencing in preclinical species and humans. *J Pharmacol Exp Ther* 2021;**379**:134−46.

22. Di JX, Wu KZ, Hou P, Corpstein CD, Xu Y, Li T. Multiphysics-informed pharmacokinetic modeling of systemic exposure of intramuscularly injected LNPs. *Mol Pharm* 2023;**20**:6162−8.

23. Jaladanki CK, Gahlawat A, Rathod G, Sandhu H, Jahan K, Bharatam PV. Mechanistic studies on the drug metabolism and toxicity originating from cytochromes P450. *Drug Metab Rev* 2020;**52**:366−94.

24. Hassett KJ, Benenato KE, Jacquinet E, Lee A, Woods A, Yuzhakov O, et al. Optimization of lipid nanoparticles for intramuscular administration of mRNA vaccines. *Mol Ther Nucleic Acids* 2019;**15**:1−11.

25. Benenato KE, Kumarasinghe ES, Mark C, inventor. Compounds and compositions for intracellular delivery of therapeutic agents. *Int Patent WO2017049245A2* 2017 Mar 23.

26. U.S. Food and Drug Administration. NDA 210922−patisiran−cross-discipline team leader review. 2018.

27. Eberhardt J, Santos-Martins D, Tillack AF, Forli S. AutoDock Vina 1.2.0: new docking methods, expanded force field, and python bindings. *J Chem Inf Model* 2021;**61**:3891−8.

28. Trott O, Olson AJ. AutoDock Vina: improving the speed and accuracy of docking with a new scoring function, efficient optimization, and multithreading. *J Comput Chem* 2010;**31**:455−61.

29. Bencharit S, Morton CL, Xue Y, Potter PM, Redinbo MR. Structural basis of heroin and cocaine metabolism by a promiscuous human drug-processing enzyme. *Nat Struct Mol Biol* 2003;**10**:349−56.

30. Bencharit S, Edwards CC, Morton CL, Howard-Williams EL, Kuhn P, Potter PM, et al. Multisite promiscuity in the processing of endogenous substrates by human carboxylesterase 1. *J Mol Biol* 2006;**363**:201−14.

31. Nemukhin AV, Grigorenko BL, Morozov DI, Kochetov MS, Lushchekina SV, Varfolomeev SD. On quantum mechanical−molecular mechanical (QM/MM) approaches to model hydrolysis of acetylcholine by acetylcholinesterase. *Chem Biol Interact* 2013;**203**:51−6.

32. Qiao Y, Han KL, Zhan CG. Reaction pathways and free energy profiles for cholinesterase-catalyzed hydrolysis of 6-monoacetylmorphine. *Org Biomol Chem* 2014;**12**:2214−27.

33. Yao JZ, Chen XB, Zheng F, Zhan CG. Catalytic reaction mechanism for drug metabolism in human carboxylesterase-1: cocaine hydrolysis pathway. *Mol Pharm* 2018;**15**:3871−80.

34. Figueiredo PR, González RD, Carvalho ATP. Human carboxylesterase 2 in cocaine metabolism. *Mol Catal* 2021;**515**:111938.

35. Himo F, de Visser SP. Status report on the quantum chemical cluster approach for modeling enzyme reactions. *Commun Chem* 2022;**5**:1−4.

36. Hu CH, Brinck T, Hult K. *Ab initio* and density functional theory studies of the catalytic mechanism for ester hydrolysis in serine hydrolases. *Int J Quan Chem* 1998;**69**:89−103.

37. Rauwerdink A, Kazlauskas RJ. How the same core catalytic machinery catalyzes 17 different reactions: the serine-histidine-aspartate catalytic triad of α/β-hydrolase fold enzymes. *ACS Catal* 2015;**5**:6153−76.

38. Hawkins PCD. Conformation generation: the state of the art. *J Chem Inf Model* 2017;**57**:1747−56.

39. Bannwarth C, Caldeweyher E, Ehlert S, Hansen A, Pracht P, Seibert J, et al. Extended tight-binding quantum chemistry methods. *Wires Comput Mol Sci* 2021;**11**:e1493.

40. Spicher S, Grimme S. Robust atomistic modeling of materials, organometallic, and biochemical systems. *Angew Chem* 2020;**132**:15795−803.

41. Bannwarth C, Ehlert S, Grimme S. GFN2-xTB−an accurate and broadly parametrized self-consistent tight-binding quantum chemical method with multipole electrostatics and density-dependent dispersion contributions. *J Chem Theor Comput* 2019;**15**:1652−71.

42. Stephens PJ, Devlin FJ, Chabalowski CF, Frisch MJ. Ab initio calculation of vibrational absorption and circular dichroism spectra using density functional force fields. *J Phys Chem* 1994;**98**:11623−7.

43. Grimme S, Antony J, Ehrlich S, Krieg H. A consistent and accurate *ab initio* parametrization of density functional dispersion correction (DFT-D) for the 94 elements H-Pu. *J Chem Phys* 2010;**132**:154104.

44. Zhao Y, Truhlar DG. The M06 suite of density functionals for main group thermochemistry, thermochemical kinetics, noncovalent interactions, excited states, and transition elements: two new functionals and systematic testing of four M06-class functionals and 12 other functionals. *Theor Chem Acc* 2008;**120**:215−41.

45. Scalmani G, Frisch MJ. Continuous surface charge polarizable continuum models of solvation. I. General formalism. *J Chem Phys* 2010;**132**:114110.

46. Marenich AV, Cramer CJ, Truhlar DG. Universal solvation model based on solute electron density and on a continuum model of the

solvent defined by the bulk dielectric constant and atomic surface tensions. *J Phys Chem B* 2009;**113**:6378−96.

47. Scott AP, Radom L. Harmonic vibrational frequencies: an evaluation of Hartree−Fock, Møller−Plesset, quadratic configuration interaction, density functional theory, and semiempirical scale factors. *J Phys Chem* 1996;**100**:16502−13.

48. Lu T, Chen QX. Shermo: a general code for calculating molecular thermochemistry properties. *Comput Theor Chem* 2021;**1200**:113249.

49. Chou WC, Cheng YH, Riviere JE, Monteiro-Riviere NA, Kreyling WG, Lin Z. Development of a multi-route physiologically based pharmacokinetic (PBPK) model for nanomaterials: a comparison between a traditional *versus* a new route-specific approach using gold nanoparticles in rats. *Part Fibre Toxicol* 2022;**19**:47.

50. Akinc A, Querbes W, De S, Qin J, Frank-Kamenetsky M, Jayaprakash KN, et al. Targeted delivery of RNAi therapeutics with endogenous and exogenous ligand-based mechanisms. *Mol Ther* 2010; **18**:1357−64.

51. Jayaraman M, Ansell SM, Mui BL, Tam YK, Chen JX, Du XY, et al. Maximizing the potency of siRNA lipid nanoparticles for hepatic gene silencing *in vivo*. *Angew Chem Int Ed Engl* 2012;**51**:8529−33.

52. Semple SC, Akinc A, Chen JX, Sandhu AP, Mui BL, Cho CK, et al. Rational design of cationic lipids for siRNA delivery. *Nat Biotechnol* 2010;**28**:172−6.

53. Jouhet J. Importance of the hexagonal lipid phase in biological membrane organization. *Front Plant Sci* 2013;**4**.

54. Zhang YB, Sun CZ, Wang C, Jankovic KE, Dong YZ. Lipids and lipid derivatives for RNA delivery. *Chem Rev* 2021;**121**:12181−277.

55. Semple SC, Klimuk SK, Harasym TO, Dos Santos N, Ansell SM, Wong KF, et al. Efficient encapsulation of antisense oligonucleotides in lipid vesicles using ionizable aminolipids: formation of novel small multilamellar vesicle structures. *Biochim Biophys Acta BBA - Biomembr* 2001;**1510**:152−66.

56. Glassman PM, Balthasar JP. Physiologically-based pharmacokinetic modeling to predict the clinical pharmacokinetics of monoclonal antibodies. *J Pharmacokinet Pharmacodyn* 2016;**43**:427−46.

57. Li Z, Shah DK. Two-pore physiologically based pharmacokinetic model with *de novo* derived parameters for predicting plasma PK of different size protein therapeutics. *J Pharmacokinet Pharmacodyn* 2019;**46**:305−18.

58. Hajj KA, Ball RL, Deluty SB, Singh SR, Strelkova D, Knapp CM, et al. Branched-tail lipid nanoparticles potently deliver mRNA *in vivo* due to enhanced ionization at endosomal pH. *Small* 2019;**15**: 1805097.

59. Zhao XW, Chen JJ, Qiu M, Li YM, Glass Z, Xu QB. Imidazole-based synthetic lipidoids for *in vivo* mRNA delivery into primary T lymphocytes. *Angew Chem Int Ed Engl* 2020;**59**:20083−9.

60. Kauffman KJ, Dorkin JR, Yang JH, Heartlein MW, DeRosa F, Mir FF, et al. Optimization of lipid nanoparticle formulations for mRNA delivery *in vivo* with fractional factorial and definitive screening designs. *Nano Lett* 2015;**15**:7300−6.

61. Dilliard SA, Cheng Q, Siegwart DJ. On the mechanism of tissue-specific mRNA delivery by selective organ targeting nanoparticles. *Proc Natl Acad Sci U S A* 2021;**118**:e2109256118.

62. Lian JH, Nelson R, Lehner R. Carboxylesterases in lipid metabolism: from mouse to human. *Protein Cell* 2018;**9**:178−95.

63. Liederer BM, Borchardt RT. Enzymes involved in the bioconversion of ester-based prodrugs. *J Pharm Sci* 2006;**95**:1177−95.

64. Wubbels GG. The Bell−Evans−Polanyi principle and the regioselectivity of electrophilic aromatic substitution reactions. *Tetrahedron Lett* 2015;**56**:1716−9.

65. Wubbels GG. Use of the Bell−Evans−Polanyi principle to predict regioselectivity of nucleophilic aromatic photosubstitution reactions. *Tetrahedron Lett* 2014;**55**:5066−9.

66. Stein Y, Halperin G, Stein O. Biological stability of [3H]cholesteryl oleyl ether in cultured fibroblasts and intact rat. *FEBS Lett* 1980;**111**: 104−6.

67. Apgar JF, Tang JP, Singh P, Balasubramanian N, Burke J, Hodges MR, et al. Quantitative systems pharmacology model of hUGT1A1-modRNA encoding for the UGT1A1 enzyme to treat Crigler−Najjar syndrome type 1. *CPT Pharmacomet Syst Pharmacol* 2018;**7**:404−12.

68. Klein S, Mason A, Lockard G, Cantrell V, Li SP, Patel K, et al. Models for drug individualization: patient to population level. In: Amponsah SK, Pathak YV, editors. *Recent advances in therapeutic drug monitoring and clinical toxicology*. Cham: Springer International Publishing; 2022. p. 303−22.

69. Shebley M, Sandhu P, Emami Riedmaier A, Jamei M, Narayanan R, Patel A, et al. Physiologically based pharmacokinetic model qualification and reporting procedures for regulatory submissions: a consortium perspective. *Clin Pharmacol Ther* 2018;**104**:88−110.

70. Jeon JY, Ayyar VS, Mitra A. Pharmacokinetic and pharmacodynamic modeling of siRNA therapeutics—a minireview. *Pharm Res (N Y)* 2022;**39**:1749−59.

71. Fairman K, Li M, Ning B, Lumen A. Physiologically based pharmacokinetic (PBPK) modeling of RNAi therapeutics: opportunities and challenges. *Biochem Pharmacol* 2021;**189**:114468.

72. Mihaila R, Ruhela D, Keough E, Cherkaev E, Chang S, Galinski B, et al. Mathematical Modeling: a tool for optimization of lipid nanoparticle-mediated delivery of siRNA. *Mol Ther Nucleic Acids* 2017;**7**:246−55.

73. Ligon TS, Leonhardt C, Rädler JO. Multi-level kinetic model of mRNA delivery *via* transfection of lipoplexes. *PLOS ONE* 2014;**9**: e107148.

74. Bruininks BM, Souza PC, Ingolfsson H, Marrink SJ. A molecular view on the escape of lipoplexed DNA from the endosome. *Elife* 2020;**9**: e52012.

75. Chakrabarti A, Podder SK. Complex carbohydrate-lectin interaction at the interface: a model for cellular adhesion. I. Effect of vesicle size on the kinetics of aggregation between a fatty acid conjugate of lectin and a liposomal asialoganglioside. *Biochim Biophys Acta BBA - Biomembr* 1990;**1024**:103−10.

76. Qiu M, Tang Y, Chen JJ, Muriph R, Ye ZF, Huang CF, et al. Lung-selective mRNA delivery of synthetic lipid nanoparticles for the treatment of pulmonary lymphangioleiomyomatosis. *Proc Natl Acad Sci U S A* 2022;**119**:e2116271119.

77. Kawakami S, Hashida M. Targeted delivery systems of small interfering RNA by systemic administration. *Drug Metab Pharmacokinet* 2007;**22**:142−51.

78. Siegbahn PEM, Himo F. Recent developments of the quantum chemical cluster approach for modeling enzyme reactions. *JBIC J Biol Inorg Chem* 2009;**14**:643−51.

79. Cheng YH, He C, Riviere JE, Monteiro-Riviere NA, Lin Z. Meta-analysis of nanoparticle delivery to tumors using a physiologically based pharmacokinetic modeling and simulation approach. *ACS Nano* 2020;**14**:3075−95.

80. Afantitis A, Melagraki G, Isigonis P, Tsoumanis A, Varsou DD, Valsami-Jones E, et al. NanoSolveIT project: driving nanoinformatics research to develop innovative and integrated tools for *in silico* nanosafety assessment. *Comput Struct Biotechnol J* 2020;**18**:583−602.

81. Wang W, Ye ZYF, Gao HL, Ouyang DF. Computational pharmaceutics—a new paradigm of drug delivery. *J Control Release* 2021;**338**:119−36.